Scaling Rules for Microrobots with Full Energetic Autonomy

Erwin van Renselaar[1], Benedikt Keitel[2], Mehmet Dinc[3], Boris Mizaikoff[2,3], Arturo Susarrey-Arce[4], Han J. G. E. Gardeniers[4], Leon Abelmann[5], and Islam S. M. Khalil[1]

***Abstract*— There is an increasing need for wireless autonomous micro electromechanical systems (MEMS) and microrobots that can perform various functions such as sensing, diagnosis, locomotion, actuation, implantation, material removal, manipulation, and localized drug delivery. A major problem with these systems is the production, storage, and transduction of power at the micro scale. In addition, these miniature devices cannot use existing battery packs that are commonly used to power electronic devices. These MEMS and microrobots need on-board power sources that are miniaturized to their size. Together with the energy of an external source, some basic functions of microrobots can be powered simultaneously. This study seeks to develop a theoretical framework based on a chemo-electromagnetic model for use in the design of microrobots with full energetic autonomy. We first conceive a microrobot design and derive its mathematical model; the design consists of an on-board fuel generator, electrochemical device, electromagnetic device, and a locomotion mechanism. Then we present numerical simulations to show the relationship between the consumption rate of the H_2 source, power density, and angular and translational velocities at low Reynolds number. We find that power density decreases approximately linearly with the diameter, while the relative velocity with respect to the body-length is approximately inversely proportional to the size, making downscaling favourable for this class of untethered devices.**

I. INTRODUCTION

Since Purcell's 1976 lecture on "*Life at low Reynolds number*" [1], and particularly in the last two decades, steady progress in imaging and microfabrication instrumentation has allowed us to create robotic systems at the micro scale [2], [3]. Feynman believed that machines could eventually be built on the scale of a human cell [4] and nature has inspired us to realize these machines in terms of locomotion methods, processes, materials, and designs. Nature's designs can be observed and theoretically understood in living systems, and this provides an approach for developing such robots and untethered devices (UDs). Despite the vast potential rewards of these microrobots and UDs, they currently do not meet our expectations because they directly transduce energy from external sources into mechanical energy. This means they bypass the production of electric energy, which is needed to power basic functions. We have been able to mimic the geometric features and basic functions of microfabricated instruments [5], [6], but have been unable to translate them into real-world applications. The main function we have not been able to implement on the micro scale is energy autonomy.

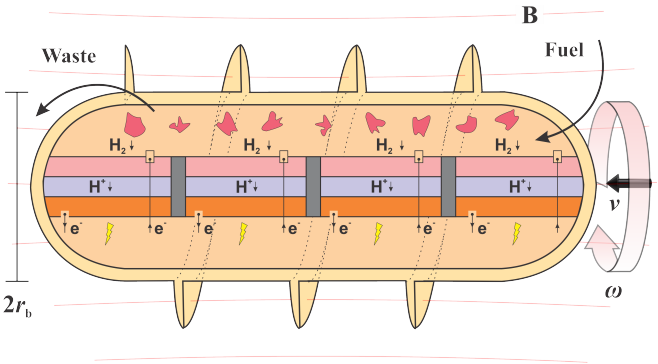

Fig. 1: A schematic representation of the untethered device (UD) indicates the end-to-end relationship between the radius, r_b, and the maximum translational speed, $\boldsymbol{v}$. On-board hydrogen production provides micro fuel cells with anodic fuel for electricity generation. The drawn current by micro coils (not shown) connected with the fuel cells provides an independent magnetic dipole moment, allowing the helical body of the UD to rotate under the influence of a *uniform static* magnetic field (red lines).

Long-term power supplies are currently obtained by employing patterned stimulus-responsive materials within their structure [6]. These materials can change their mechanical and chemical characteristics when exposed to heat [7], light [8], ultrasound fields [9], magnetic fields [10], and electric fields [11]. These stimuli, either alone or in combination, can power limited tasks such as locomotion and simple transportation. In practice, several functions should be available and should be independently powered to improve an intended task. This method of harnessing and transducing energy has given microrobots some limited functioning but is not sufficient for autonomous operation. Using an external power source [12] just to drive MEMS reduces their functionality, meaning they can only execute simple tasks. To date, mechanical energy has been directly transduced from external sources for wireless locomotion and most research has been performed *in vitro*. However, the most promising function for microrobots is in localized drug delivery and wireless diagnostics [3], [13]. Nearly every design of untethered MEMS relies on bypassing the production of electricity, thereby limiting the functions that are needed for significant improvement. This technology is

[1]E. van Renselaar and I. S. M. Khalil are with the Department of Biomechanical Engineering, University of Twente, 7500 AE Enschede, The Netherlands (e-mail: i.s.m.khalil@utwente.nl).

[2]B. Keitel and B. Mizaikoff are with the Institute of Analytical and Bioanalytical Chemistry, Ulm University, 89081 Ulm, Germany.

[3]M. Dinc and B. Mizaikoff are with Hahn-Schickard, 89077 Ulm, Germany.

[4]A. Susarrey-Arce and H. J. G. E. Gardeniers are with the Department of Mesoscale Chemical Systems, University of Twente, 7500 AE Enschede, The Netherlands.

[5]L. Abelmann is with KIST Europe, 66123 Saarbrucken, Germany.

978-1-6654-5973-0/22/$31.00 ©2022 IEEE

not yet advanced enough to translate microrobots into real-world applications. In contrast, we have known that living systems can transduce and connect chemical, electrical, and mechanical energy. However, a system capable of using this biological pathway has not yet been explored at the submillimeter and micro scales. Therefore, the aim of this study is to conceive a design of a UD with full energetic autonomy to gain insight on how fuel consumption and scaling rules affect its swimming velocity.

In this work, we begin by introducing a conceptual design of an assembled-MEMS UD capable of conducting consecutive energy transductions; these are, chemical-to-electrical energy using a micro fuel generator (MFG) and an electrochemical device and electrical-to-mechanical energy using MEMS for magnetic dipole generation and locomotion (Fig. 1). Using this chemo-electromechanical pathway enables us to derive the governing dynamics of the UD and provide an end-to-end relationship between the inputs (i.e., size and anodic fuel production rate) and the outputs (i.e., velocities, and electrical and hydrodynamic efficiencies). The remainder of this paper is organized as follows: Section II provides descriptions of the fundamental physics that governs energy conversion in the UD and energy consumption by its loads, and validation of the numerical model of the electrochemical system. The numerical simulations of the end-to-end process are provided in Section III and provide discussions pertaining to the limitations of downscaling. Finally, Section IV concludes and provides direction for future work.

II. CONCEPTUAL DESIGN AND GOVERNING EQUATIONS

We consider a UD containing an MFG, a micro fuel cell (MFC), and a three-dimensional (3-D) tri-axial micro electromagnetic coil. The UD, with radius r_{b} and length L, is surrounded by a viscous fluid (e.g., water, bodily fluids, or liquid waste) characterized by low Reynolds (Re) number, while lying in a *uniform static* magnetic field, $\mathbf{B}$. Upon the addition of the fluid to the MFG the H_2 is produced and an oxidation reaction occurs at the anode of the MFC, powering the tri-axial coil and rotating at an angular velocity $\boldsymbol{\omega}$. In what follows, we discuss the general scheme and the fundamental physics pertaining to its interconnected components.

A. Microrobot Utilizing Calcium Hydride for Electricity Generation and External Field Assisted Motion

We see in the literature that a number of designs have been proposed and tested for UDs. They can be sorted in categories based on the type of external stimuli (e.g., magnetic, acoustic, thermal, or hybrid). Unlike externally-driven UDs an on-board fuel generator and fuel cell allow us to provide an independent time-varying magnetic dipole moment, $\mathbf{m}$. Once equipped with this dipole moment, we can use a static external magnetic field to produce a magnetic torque. This torque can be applied to rotate the UD about any desired rotation axis based on the current drawn by each coil of the tri-axial configuration. We can simplify the actuation problem enormously by relying on an external source only for field-assisted motion. Note also that as soon as electricity is generated on-board the UD, we obtain a more effective means for powering other basic functionalities.

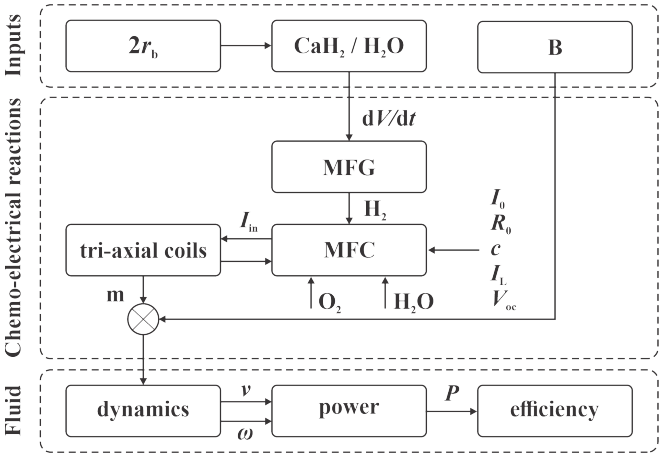

Fig. 2: The end-to-end process is modelled to predict the rotational and translational velocity, $\boldsymbol{\omega}$ and $\boldsymbol{v}$, for a given body size $2r_{\mathrm{b}}$ of the untethered device (UD) and a static magnetic field $\mathbf{B}$. The size of the fuel cell dictates the generated current, and thus the consumption rate of the H_2 fuel from CaH_2 source. Open-circuit voltage, V_{oc}, current, I_0, and resistance, R_0, characterize the performance of the micro fuel cell, MFC. A magnetic moment, $\mathbf{m}$, large enough to provide magnetic torque would rotate the UD at angular velocity $\boldsymbol{\omega}$.

Fig. 2 shows a diagram of our concept. The size of the UD in terms of r_{b} dictates the volume of the hydrogen source (e.g., metal hydrides) which undergoes hydrolysis reactions at room temperature. The external field strength, which is also another input in our model, dictates the magnetic torque that will be ultimately balanced by the drag torque and determines the angular velocity of the UD. Once the MFC and its tri-axial electromagnetic coils are powered, a magnetic torque is produced and rotates the UD. The resistance to rotational motion scales as $\|\boldsymbol{\tau}_{\mathrm{d}}\| \sim r_{\mathrm{b}}^3$, while the magnetic torque scales as $\|\boldsymbol{\tau}_{\mathrm{m}}\| \sim r_{\mathrm{b}}^2$ for a given field strength and electromagnet parameters. Therefore, the angular velocity of the UD is expected to scale as $\|\boldsymbol{\omega}\| \sim r_{\mathrm{b}}^{-1}$. To gain sufficient insights into the magnetic torque we must understand the energy balance of the MFG and MFC, and then transfer the MFC's power to the tri-axial coils to achieve locomotion.

B. Open-Circuit Voltage and Energy Balance

It has been shown that when water is pumped into a Calcium Hydride (CaH_2) chamber such that the pressure of the produced H_2 regulates the water flow, the generated H_2 can be continuously supplied to the anode of the MFC [14]. In this case, an oxidation reaction and a reduction reaction occur at the anode and cathode, respectively, and we have

$$\mathrm{H_2} \longrightarrow 2\mathrm{H^+} + 2\mathrm{e^-}; \tag{1}$$

$$\mathrm{O_2} + 4\mathrm{e^-} + 4\mathrm{H^+} \longrightarrow 2\mathrm{H_2O}. \tag{2}$$

The potential at the anode, E_{A}^0, is 0 V while the potential at the cathode, E_{C}^0, is 1.23 V. Therefore, the standard cell

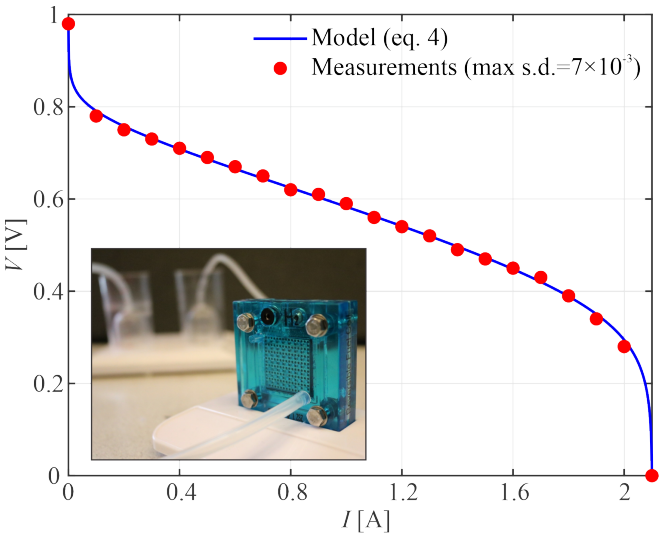

Fig. 3: V-I characteristics of a fuel cell is measured and calculated numerically using Equation (4). The numerical V-I characteristics is determined using $I_0 = 3.19 \times 10^{-5}$ A, $R_e = 0.33\ \Omega$, $c = 1.88 \times 10^{-4}$ V.K^{-1}, $I_L = 0.97$ A, and $V_{oc} = 0.96$ V. This model, based on multiple voltage losses, describes the V-I relationship of the fuel cell (in the inset image) within measurement error.

potential is given by $E_e^0 = E_C^0 - E_A^0 = 1.23$ V. Since E_e^0 is valid at standard temperature and pressure, a correction for temperature and pressure is used as follows:

$$E_N = E_e^0 + \frac{RT}{zF} \ln\left(\frac{(P_{H_2})^2 P_{O_2}}{(P_{H_2O})^2}\right), \quad (3)$$

where E_N is the Nernst potential in equilibrium, R is the molar gas constant, T is the temperature of the MFC, F is Faraday constant, and z is the number of electrons transferred in one complete reaction (i.e., $z = 4$) [15]. Furthermore, P_{H_2} and P_{O_2} are the fugacities of H_2 and O_2, respectively. In the range of pressures relevant for this experiment, close to atmospheric pressure, the fugacity is approximately equal to the partial pressure of each gas, in bar. Finally, P_{H_2O}, since it is produced as a fluid, is the activity of water, which is identically equal to one.

When a current is generated in the MFC, multiple voltage losses occur. Due to imperfections in the MFC, more specifically the crossover of H_2 in open-circuit, an initial voltage loss, E_c, is treated as a dependent parameter on the MFC [15]. Second, due to the activation barrier that must be overcome in a reaction, a voltage loss, V_{act}, occurs [16] [17]. Third, since the fuel itself is part of the electrical circuit as well, with non-zero resistance, an Ohmic voltage drop due to its internal, resistance, V_{ohm}, occurs [17], [18]. The final voltage loss, V_{con}, occurs mostly at high currents, where the diffusion of H_2 and O_2 limits the fuel supply to the MFC [17], [18]. Thus, E_{MFC} can be expressed as

$$E_{MFC} = \Delta E - \frac{2RT}{e_A F} \text{arsinh}\left(\frac{I}{2I_0}\right) - R_e I - cT \ln(\alpha), \quad (4)$$

where $\Delta E = E_N - E_c$ and $\alpha = I_L/(I_L - I)$, e_A is the number of electrons transferred at the anode, I is the generated current, I_0 is the exchange current, R_e is the internal resistance of the MFC, and I_L is the limiting current. Often we can empirically estimate the parameter c, since the governing equation does not correlate to experimental data [17]. It is important to note here that the derivation of V_{act} from the Butler-Volmer equation depends on the charge transfer coefficients $\in [0, 1]$ being equal to 0.5. Although these are often not precisely known, this assumption is justified in previous studies [19]. Note also that I depends on the size of the UD and the external electrical load. Once the electrical load is connected to the MFC that is supplied constantly by H_2, the rate of energy consumption will depend on the external load. Therefore, to ensure that Equation (4) can be further generalized and used to predict the relation between I and the corresponding change in E_{MFC}, we determine the V-I characteristics experimentally.

Fig. 3 shows the V-I characteristics of a fuel cell connected to a current load. The measurement is performed using a Solar Hydrogen Science Kit (FCJJ-16, Horizon Fuel Cell Europe, Czech Republic). The fuel cell (Fig. 3, inset image) is connected in series to an electrical load (VOLTCRAFT V-Charge 60 DC Multifunctional Model Kit Charge) to control the current drawn. A DC power supply is used to power this electrical load and multimeters are used to concurrently measure the voltage and the current through the fuel cell. Equation (4) predicts the V-I characteristics for $I_0 = 3.19 \times 10^{-5}$ A, $R_e = 0.33\ \Omega$, $c = 1.88 \times 10^{-4}$ V.K^{-1}, $I_L = 0.97$ A, and $E_c = 0.96$ V. Fig. 3 indicates close agreement between the numerical results (blue curve) of Equation (4) and experimental data (red points). With this agreement between the theoretical results and measurements, we can maximize power transfer to the tri-axial electromagnetic coils by matching its impedance with the MFC.

C. Tri-Axial Electromagnetic Coils

Now suppose we achieve a current density J when the MFC is operated at maximum power. We will need to achieve impedance-matching between the MFC and the tri-axial coils, such that

$$R_w = \frac{E_{MFC}}{\pi J r_b^2} = \rho_w \frac{l_w}{\pi r_w^2}, \quad (5)$$

where ρ_w is the resistivity of the material of the wire of the coils and l_w is the length of the wire. Further, r_w is the radius of the wire. Note that the resistance of the tri-axial coil, R_w, in Equation (5) is calculated for maximum power. A magnetic torque large enough to rotate the UD and its tri-axial coils with respect to the external magnetic field would cause flux changes in the coils and produce back emf. Therefore, the effective currents are given by

$$I_{eff,i} = \pi r_b^2 J - \frac{2N_i B S_i \sin(\phi_i)\omega_i}{R_w} \quad \text{for} \quad i = 1, 2, 3, \quad (6)$$

where N_i and S_i are the number of turns and the surface area of the ith coil, respectively, ϕ_i is the angle of the ith electromagnetic coil with respect to a frame of reference and ω_i is the angular velocity of the UD around the ith axis.

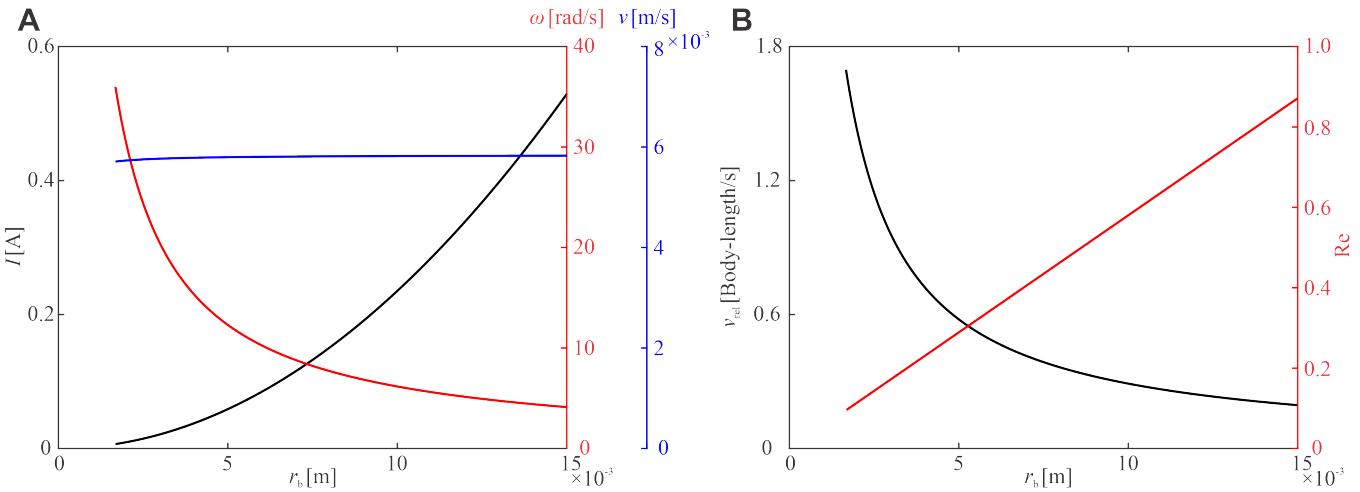

Fig. 4: The total current drawn by on-board tri-axial electromagnetic coils, I, angular velocity, $\|\boldsymbol{\omega}\|$, and translational speed, $\|\boldsymbol{v}\|$, are calculated for different sizes of the untethered device (UD) in the $1.7 \leq r_{\mathrm{b}} \leq 15$ mm range. Parameters: $B = 1.5$ T (within the range of a magnetic resonance imaging system), $\eta = 200$ mPa.s, $\rho = 997$ kg.m^{-3}. (A) The current drawn by the tri-axial coils decreases as size decreases, from 0.5 A to 7 mA. The angular velocity increases significantly by downscaling the UD, from 4 to 36 rad.s^{-1}, while the translational velocity only slightly decreases, from 5.8 to 5.7 mm.s^{-1}. (B) The relative velocity, $v_{\mathrm{rel}} = \|\boldsymbol{v}\|/(2r_{\mathrm{b}})$, increases from 0.2 to 1.8 body lengths per second as the size of the UD decreases. Over the entire range of r_{b}, we have $\mathrm{Re} < 1$.

D. Hydrodynamics and Equation of Motion

For translating the UD using a static magnetic field, at least two requirements are needed. The first is a geometry that allows for drag-based propulsion upon rotation with respect to a desired rotation axis (i.e., the long axis of the helical body). The second requirement is to generate a dipole moment using the current drawn by the electromagnetic coils using Equation (6) in a time-periodic manner. This moment has to be rotated about a desired axis of rotation. In this case, $\boldsymbol{\tau}_{\mathrm{m}}$ will balance $\boldsymbol{\tau}_{\mathrm{d}}$, resulting in an $\boldsymbol{\omega}$ and, because of the helical shape, a translational velocity, $\boldsymbol{v}$. This relation holds for low-Re, where $\mathrm{Re} = 2r_{\mathrm{b}}\rho\|\boldsymbol{v}\|/\eta$ for a fluid with density ρ and viscosity η. Then the torque balance is given by

$$NS\mathbf{I}_{\mathrm{eff}} \times \mathbf{B} = 8\pi\eta r_{\mathrm{b}}^3 \boldsymbol{\omega}, \tag{7}$$

where $\mathbf{I}_{\mathrm{eff}}$ is a vector of the drawn currents by the tri-axial electromagnetic coils given by Equation (6). This completes the rotational dynamics of the UD and the transduction of electrical energy into work. When the MFC is provided with a constant supply of H_2 fuel by the MFG, then the rate of consumption of this fuel will depend on the current load of the tri-axial coils. Using Equation (7), the rotational velocity, $\boldsymbol{\omega}$, around the longitudinal axis can be calculated. To translate this rotation into a forward motion, a simplified model of a rigid helical body in low-Re is used [20]. To gain insight into how much energy is lost in the system, and specifically in which transition, efficiencies are particularly useful. Three different powers are distinguished. The first is the electrical power P_E, calculated with $P_{\mathrm{E}} = E_{\mathrm{MFC}} I$. The second is the rotational power P_{R}, determined with $P_{\mathrm{R}} = \boldsymbol{\tau}_{\mathrm{m}}^T \boldsymbol{\omega}$. The third is the translational power P_{T}, which is calculated as $P_{\mathrm{T}} = 6\pi\eta r_{\mathrm{b}}\|\boldsymbol{v}\|^2$. The efficiency from the electrical domain to the rotational domain is given as $\eta_{\mathrm{R}} = P_{\mathrm{R}}/P_{\mathrm{E}} \times 100\%$. The efficiency from electrical energy to forward motion can be calculated as $\eta_{\mathrm{T}} = P_{\mathrm{T}}/P_{\mathrm{E}} \times 100\%$.

E. Consumption rates

The fuel cell needs both H_2 and O_2, with the former theoretically supplied by the hydrolysis of CaH_2. In this case water is needed for the hydrolysis. The consumption rate of CaH_2, C_{C}, can be calculated with $C_{\mathrm{C}} = Im_{\mathrm{C}}/(4F\rho_{\mathrm{C}})$. The consumption rate of H_2O and C_{H}, is calculated with $C_{\mathrm{H}} = Im_{\mathrm{H}}/(2F\rho_{\mathrm{H}})$. The consumption rate of O_2 and C_{O}, can be determined with $C_{\mathrm{O}} = Im_{\mathrm{O}}/(4F)$. Here, m_{C} and m_{H} are the molar masses of CaH_2 and H_2, respectively, ρ_{C} and ρ_{H} are their respective densities. For O_2 its molar volume m_{O} is used.

III. NUMERICAL SIMULATIONS AND DOWNSCALING

The governing equations of the UD are solved analytically using Equations (1)-(7) based on the characterized parameters of the MFC of the I-V curve. The implementation of these equations is shown in Fig. 2 and the continuity of the model allows us to find the relationship between any given size of a UD, an external magnetic field, and the H_2 source.

A. Numerical Example

In order to obtain theoretical results, we first discuss the following design example: In an experimental setup with a membrane electrode assembly of 3×3 cm^2, the peak power is determined at $E_{\mathrm{MFC}} = 0.423$ V and $I = 0.674$ A, which provides $J = 749$ A.m^{-2}. Next, we determine the smallest r_{b} (i.e., $r_{\mathrm{b,min}}$) possible for the capsule to contain the coils. To achieve impedance-matching in Equation (5), r_{w} is chosen to have a linear relationship with r_{b}, with unknown scaling factor β. Since a circular coil is assumed to be used, $l_{\mathrm{w}} = 2\pi N r_{\mathrm{c}}$. As for the wire, it is assumed to be made of

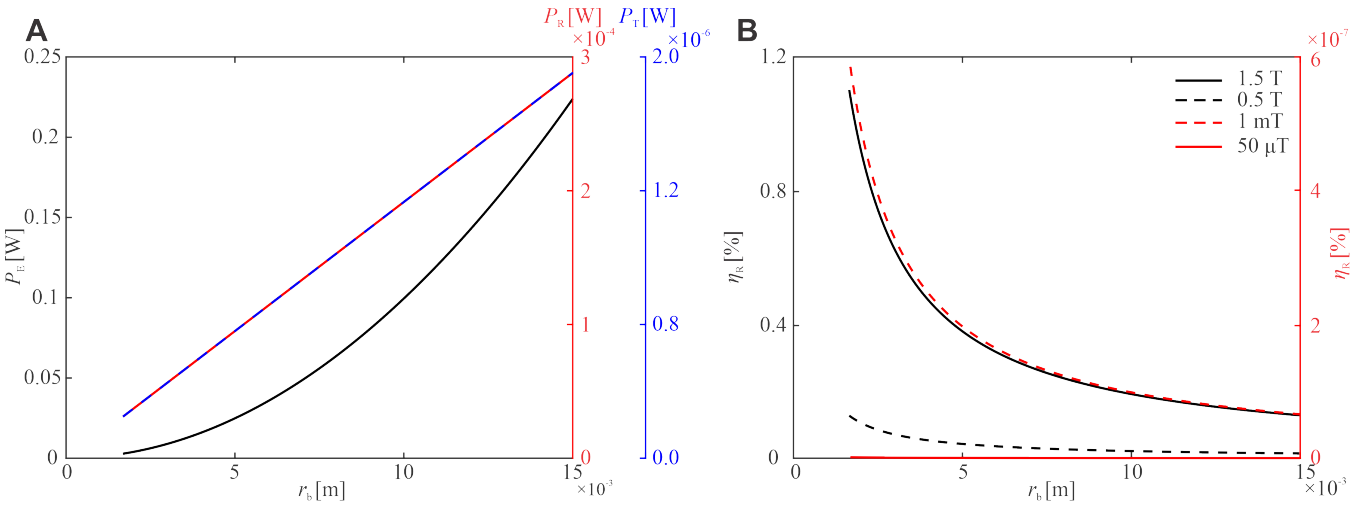

Fig. 5: The size and the external magnetic field strength have a direct influence on the electrical power, P_{E}, rotational power, P_{R}, translational power, P_{T}, and rotational efficiency, η_{R}. Parameters: $\eta = 200$ mPa.s, $\rho = 997$ kg.m^{-3}. (A) The P_{E} decreases quadratically with the size of the UD, from 0.2W to 3mW. The P_{R} and P_{T} show a linear decrease, separated by a constant factor of 0.007. (B) Regardless of the external magnetic field strength, the UD becomes more efficient as size decreases, with the highest η_{R} equal to 1.1%.

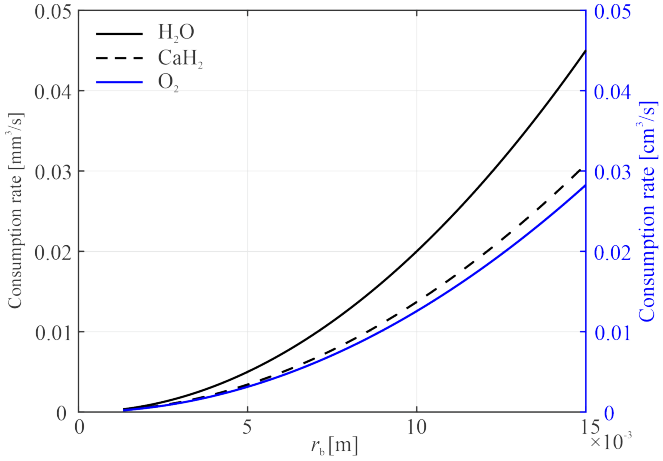

Fig. 6: The end-to-end process indicates the consumption rate of CaH_2/O_2 for the $1.7 \leq r_{\mathrm{b}} \leq 15$ mm range. The 15-mm UD consumes ~ 0.04 mm^3.s^{-1} of CaH_2 and H_2O, and ~ 0.03 cm^3.s^{-1} of O_2. These rates decrease quadratically with size to $\sim 5 \times 10^{-4}$ mm^3.s^{-1} and $\sim 4 \times 10^{-4}$ cm^3.s^{-1} at a radius of 1.7 mm.

copper, with $\rho_{\mathrm{w}} = 1.68 \times 10^{-8}$ Ω.m. The smallest value for r_{w} (i.e., $r_{\mathrm{w,min}}$) is chosen to be 5 μm.

This calculation is implemented for one resistance. However, since the design includes tri-axial coils with parallel resistances, the resistances are three times higher than the total resistance. Therefore, each coil design is made such that there is space for a coil that is three times greater than its length. To fit the coil inside one hemisphere at $r_{\mathrm{b,min}}$, r_{c} is chosen to be $(\sqrt{2}/4)r_{\mathrm{b,min}}$. The length of the coil, l_{c}, equals $(\sqrt{2}/3)r_{\mathrm{b,min}}$, but also $l_{\mathrm{c}} = 2Nr_{\mathrm{w,min}}$. The total set of constraints together with solutions for the parameters are provided in Table I. The chosen range for r_{b} is set from 1.68 mm to 15 mm. With this design, it is now possible to obtain results from the equations of motion. Besides these constraints, some other choices have been made during calculation. Since the goal is to calculate the highest velocity that can be constantly achieved, in Equation (6) all elements of ϕ are set to $\pi/2$ to maximize the back emf.

B. Current Density and Swimming Velocities

Fig. 4(A) shows the current drawn by the UD as its size decreases in the $1.68 \leq r_{\mathrm{b}} \leq 15$ mm range and for magnetic field strength of 1.5 T. A clinical magnetic resonance imaging (MRI) system can provide greater magnetic fields in access of 1.5 T and the continuity of our model allows for prediction of the behavior for any given magnetic field. We find that a UD of 3.4-mm diameter can, at maximum power, draw a current of approximately 6.7 mA, resulting in angular velocity of 36 rad.s^{-1} and translational speed of more than 5.7 mm.s^{-1}. We observe an interesting behavior in Fig. 4(B) for the relative swimming velocity of the UD. The relative velocity of a UD of 3.4-mm diameter is 8.5 times greater than that of a UD of 30-mm diameter. The relative velocity, $v_{\mathrm{rel}} = \|\boldsymbol{v}\|/2r_{\mathrm{b}}$, increases as the size decreases and swimming under the influence of a uniform static magnetic field becomes favourable as r_{b} decreases.

C. Power, Efficiencies, and Fuel Consumption Rate

In contrast to the relative swimming velocity of the UD, the bigger the UD's diameter, the greater the output it can provide. Fig. 5(A) shows that the electrical, rotational, and translational output powers of the UD increase with r_{b} for $B = 1.5$ T. One aspect of helical propulsion, which is fundamental to drag-based locomotion in low-Re, that

TABLE I: Constraint equations and their unique solutions

Constraints	Solutions
$r_{\mathrm{c}} = (\sqrt{2}/4)r_{\mathrm{b,min}}$	$\beta = 3.0 \times 10^{-3}$
$(\sqrt{2}/3)r_{\mathrm{b,min}} = 2Nr_{\mathrm{w,min}}$	$N = 79$
$r_{\mathrm{b,min}}\beta = r_{\mathrm{w,min}}$	$r_{\mathrm{c}} = 5.95 \times 10^{-4}$m
$E_{\mathrm{MFC}}/(\pi J r_{\mathrm{b}}^2) = \rho_{\mathrm{w}} l_{\mathrm{w}}/(\pi r_{\mathrm{w}}^2)$	$r_{\mathrm{b,min}} = 1.68 \times 10^{-3}$ m

TABLE II: The electrical and swimming characteristics of an untethered derive (UD) are calculated for three sizes. Hydrodynamic efficiencies, power and energy density, fuel consumption rate, and lifetime of each UD of body length, bl, are calculated for an external field of 1.5 T and fluid with viscosity of 200 mPa.s. The consumption rate of the hydrogen source and lifetime are C_{C} and t_{l}, respectively. The UD of 2.6-mm diameter is important for microrobotic applications while the UD of 30-mm diameter is relevant to active capsule endoscopes.

r_{b} [mm]	I [A]	$\|\boldsymbol{\omega}\|$ [rad/s]	$\|\boldsymbol{v}\|$ [mm/s]	v_{rel} [bl/s]	Re	P_{d} [mW/(mm^3)]	η_{R} [%]	η_{T} [%]	C_{C} [mm^3/s]	t_{l} [h]
1.68	6.7×10^{-3}	36	5.7	1.7	0.096	0.56	1.13	7.3×10^{-3}	4.3×10^{-4}	6.5
9.0	0.19	6.9	5.8	0.32	0.52	0.11	0.21	1.4×10^{-3}	1.2×10^{-2}	35
15	0.53	4.1	5.8	0.19	0.87	0.063	0.13	8.6×10^{-4}	3.3×10^{-2}	58

is particularly important is the efficient rotation. Fig. 5(B) shows that the rotational efficiency of the UD increases as size decreases regardless of the external magnetic field strength. In this case, the field strength is varied through a wide range of $50 \times 10^{-6} \leq B \leq 1.5$ T, where its limits represent earth's magnetic field and MRI's field. It is unlikely that a UD can rotate using earth's magnetic field and its size must be decreased below the range shown in Fig. 5(B). However, the efficiency is much higher for a greater magnetic field for a given UD's size. Note that η_{R} (Fig. 5(B)) and v_{rel} (Fig. 4(B)) show a similar increase as r_{b} decreases.

Fig. 6 reveals a critical aspect in the design of the UD. Since it relies on a fuel source (i.e., $\mathrm{CaH_2/O_2}$) that is limited by the size of the UD, the consumption rate will provide an estimate of its lifetime. The consumption rates of $\mathrm{H_2O}$, $\mathrm{CaH_2}$, and $\mathrm{O_2}$ decrease approximately quadratically as size decreases, while the volume available for fuel decreases proportional to r_{b}^3. Table II provides the electrical, motion, and performance characteristics of three UDs of 3.4-mm, 18-mm, and 30-mm diameter. The first has a lifetime of 6.5 h, while the much bigger UDs of 18-mm and 30-mm diameter have a lifetime of 35 and 58 h, respectively. The power density, P_{d}, shows a linear increase for decreasing r_{b}, since $P_{\mathrm{E}} \sim r_{\mathrm{b}}^2$ but the volume is proportional to r_{b}^3. These scaling rules present advantages in downscaling and are favourable for microrobots.

IV. CONCLUSIONS

The swimming velocity of a UD is effectively independent of its size and achieves maximum speed of 1.8 body lengths per second. We find that the fuel consumption rates decrease quadratically with the size of the UD. Based on these calculations, it is theoretically possible to integrate a fuel generator, an electrochemical device, and an electromagnetic system into an assembled-MEMS UD and achieve external field-assisted locomotion in low-Re. An advantage of such assembled-MEMS UD, which contains these devices inside a helical body, over externally-driven UDs is their ability to swim controllably under the influence of a uniform static magnetic field. Our theoretical predictions reveal the end-to-end process which involves the transduction of chemical to mechanical energy without bypassing the electrical energy. This unique capability will likely provide the most practical way to design microrobots and UD with multiple functionalities. We also find that this end-to-end process becomes more desirable as the size of the UD decreases, especially considering higher relative velocities, power densities, and efficiencies. In future, we will fabricate the UDs provided in Table II, validate the theoretical predictions, and apply further refinement of the UD to achieve energetic autonomy.

REFERENCES

[1] E. M. Purcell, "Life at low Reynolds number," *American Journal of Physics*, vol. 45, no.2, pp. 3-11, 1977.

[2] M. Sitti, "Voyage of the microrobots," *Nature*, vol. 458, pp. 1121–1122, 2009.

[3] B. J. Nelson, I. K. Kaliakatsos, and J. J. Abbott, "Microrobots for minimally invasive medicine," *Annu. Rev. Biomed. Eng.*, vol. 12, pp. 55–85, 2010.

[4] R. P. Feynman, "There's plenty of room at the bottom," *Engineering and Science*, vol. 23, no. 5, pp. 22-36, 1960.

[5] M. Wehner, R. L. Truby, D. J. Fitzgerald, B. Mosadegh, G. M. Whitesides, J. A. Lewis, and R. J. Wood, "An integrated design and fabrication strategy for entirely soft, autonomous robots," *Nature*, vol. 536, pp. 451–455, 2016.

[6] C. Hu, S. Pané, and B. J. Nelson, "Soft micro- and nanorobotics," *Annual Review of Control, Robotics, and Autonomous Systems*, vol. 1, pp. 53-75, 2018.

[7] B. Jeong, S. W. Kim, and B. Y. Han, "Thermosensitive sol-gel reversible hydrogels," *Advanced Drug Delivery Reviews*, vol. 64, pp. 54-62, 2012.

[8] S. Palagi et al., "Structured light enables biomimetic swimming and versatile locomotion of photoresponsive soft microrobots," *Nature Materials*, vol. 15, pp. 647–653, 2016.

[9] W. Wang, L. A. Castro, M. Hoyos, and T. E. Mallouk, "Autonomous motion of metallic microrods propelled by ultrasound," *ACS Nano*, vol. 6, no. 7, pp. 6122–6132, 2012.

[10] L. Zhang, et al., "Controlled propulsion and cargo transport of rotating nickel nanowires near a patterned solid surface," *ACS Nano*, vol. 4, pp. 6228–6234, 2010.

[11] P. Calvo-Marzal, S. Sattayasamitsathit, S. Balasubramanian, J. R. Windmiller, C. Daoa, and J. Wang, "Propulsion of nanowire diodes," *Chemical Communications*, vol. 46, no. 10, pp. 1623–1624, 2010.

[12] J. J. Abbott, E. Diller, and A. J. Petruska, "Magnetic methods in robotics," *Annual Review of Control, Robotics, and Autonomous Systems*, vol. 3, pp. 57-90, 2019.

[13] M. Sitti, H. Ceylan, W. Hu, J. Giltinan, M. Turan, S. Yim, and E. Diller, "Biomedical applications of untethered mobile milli/microrobots," *Proc. IEEE Inst. Electr. Electron. Eng.*, vol. 103, pp. 205–224, 2015.

[14] V. V. Swaminathan, L. Zhu, B. Gurau, R. I. Masel, and M. A. Shannon, "Integrated micro fuel cell with on-demand hydrogen production and passive control MEMS," *Microfluidics and Nanofluidics*, vol. 12, no. 5, pp. 735–749, 2012.

[15] U. Chakraborty, "Fuel crossover and internal current in proton exchange membrane fuel cell modeling," *Applied Energy*, vol. 163, Feb., pp. 60-62, 2016.

[16] L. W. Juang, P. J. Kollmeyer, T. M. Jahns, and R. D. Lorenz, "Improved nonlinear model for electrode voltage-current relationship for more consistent online battery system identification." in Proc. *IEEE Energy Conversion Congress and Exposition*, 2011, pp. 2628–2634.

[17] C. Spiegel, *PEM fuel cell modeling and simulation using matlab*. Massachussets, MA: Academic Press, 2008.

[18] S. V. Puranik, A. Keyhani, and F. Khorrami, "State-Space modeling of proton exchange membrane fuel cell." In Proc. *IEEE Transactions on Energy Conversion*, pp. 804-813, 2010.

[19] A. J. Bard, L. R. Faulkner, and Larry R. *Electrochemical methods: fundamentals and applications*, 2nd ed. Hoboken, NJ: John Wiley & Sons, 2001.

[20] B. de Lima Bernardo, and F. Moraes, "Simplified model for the dynamics of a helical flagellum," *American Journal of Physics*, vol. 79, no. 7, pp. 736–740, 2011.